



Reduced graphene oxide nanosheets coated with an anti-angiogenic anticancer low-molecular-weight heparin derivative for delivery of anticancer drugs



Gayong Shim^{a,1}, Ji-Young Kim^{a,1}, Jeonghoon Han^b, Seung Woo Chung^a, Soondong Lee^a, Youngro Byun^{a,b,*}, Yu-Kyoung Oh^{a,*}

^a College of Pharmacy and Research Institute of Pharmaceutical Sciences, Seoul National University, Seoul 151-742, Republic of Korea

^b Department of Molecular Medicine and Biopharmaceutical Sciences, Graduate School of Convergence Science, Seoul National University, Seoul 151-742, Republic of Korea

ARTICLE INFO

Article history:

Received 12 February 2014

Accepted 17 June 2014

Available online 26 June 2014

Keywords:

Anti-angiogenic anticancer low molecular weight heparin derivative
Reduced graphene oxide
Dispersion stability
Doxorubicin
Anticancer effect

ABSTRACT

Here, we report reduced graphene oxide (rGO) nanosheets coated with an anti-angiogenic anticancer taurocholate derivative of low-molecular-weight heparin (LHT7) as a tumor-targeting nanodelivery platform for anticancer drugs. Surface coating of LHT7 onto rGO was confirmed using fluorescein isothiocyanate-labeled LHT7, monitored as fluorescence quenching due to associated rGO. Unlike plain rGO, LHT7-coated rGO (LHT-rGO) nanosheets maintained a stable dispersion under physiological conditions for at least 24 h. Moreover, LHT-rGO provided greater loading capacity for doxorubicin (Dox) compared with uncoated rGO nanosheets. Following intravenous administration into KB tumor-bearing mice, *in vivo* tumor accumulation of LHT-rGO/Dox was 7-fold higher than that of rGO/Dox 24 h post dosing. In tumor tissues, LHT-rGO/Dox was shown to localize not to the tumor vasculature, but rather to tumor cells. Intravenously administered LHT-rGO/Dox showed the greatest anti-tumor effect in KB-bearing mice, reducing tumor volume by $92.5\% \pm 3.1\%$ compared to the untreated group 25 days after tumor inoculation. TUNEL assays revealed that the population of apoptotic cells was highest in the group treated with LHT-rGO/Dox. Taken together, our results demonstrate that LHT-rGO nanosheets confer improved dispersion stability, tumor distribution and *in vivo* antitumor effects, and may be further developed as a potential active nanoplatform of various anticancer drugs.

© 2014 Elsevier B.V. All rights reserved.

1. Introduction

Graphene-based nanomaterials have been the focus of considerable research efforts by virtue of their unique features, including optical, mechanical, chemical and thermal properties, raising tremendous interest for their potential pharmaceutical applications [1–3]. However, because graphene-based nanosheets are derived from hydrophobic graphite through chemical or physical modification, their pharmaceutical applications have been hampered by their instability under physiological conditions [4–8].

Reduced graphene oxide (rGO) nanosheets that mimic single-layered graphene nanosheets have been generated by decreasing the polar groups on graphene oxide (GO). The planar structure of rGO serves a double-edged sword: it provides a high capacity for hydrophobic interactions among various functional molecules, but it leads to

formation of aggregates with poor dispersion stability under physiological conditions [9,10].

Surface modification of rGO with synthetic polymers or biopolymers has been used to stabilize and improve the utility of rGO as nanocarriers for therapeutics [11–16]. Polyethylene glycol (PEG)-grafted rGO nanosheets have been shown to provide a high loading capacity and cellular-uptake efficiency for single-stranded RNA cargoes [12]. Functionalization of rGO with PEGylated, branched polyethylenimine has been reported to promote cytosolic drug delivery through photothermal disruption of endosomes [13]. Biopolymers, such as hyaluronic acid derivatives [14], dextran [15], and heparin [16], have been studied as surface coatings for rGO. However, most molecules used for surface coating do not possess intrinsic anticancer activity. If an rGO surface coating material were capable of providing both stabilization and anticancer effects, it might enhance the suitability of rGO for anticancer drug delivery applications.

Derivatives of low-molecular-weight heparin (LMWH), a highly sulfated polysaccharide, have been studied as potential anticancer agents [17]. Among LMWH derivatives, LMWH-taurocholate conjugate 7 (LHT7), in which LMWH is conjugated to taurocholic acid at a molar

* Corresponding authors. Tel.: +82 2 880 2490; fax: +82 2 882 2493.

E-mail addresses: yrbyun@snu.ac.kr (Y. Byun), ohyk@snu.ac.kr (Y.-K. Oh).

¹ These authors equally contributed to this work.

ratio of 1 to 7, has been suggested as a prominent anticancer drug with significantly enhanced anti-angiogenic activity and reduced anti-coagulant activity [18]. Recently, liposomal co-delivery of LHT7 and suberanilohydroxamic acid, a histone deacetylase inhibitor, was shown to provide synergistic anticancer activity [19].

Taking advantage of the anti-angiogenic anticancer activity of LHT7 and its highly sulfated polysaccharide and taurocholate moieties, we hypothesized that surface coating of rGO with LHT7 would improve the dispersion stability of these nanosheets and enhance the anticancer efficacy upon delivery with a chemical anticancer drug. In this study, we thus investigated whether LHT7 affected the dispersion stability of rGO and evaluated the *in vivo* distribution and antitumor effects of LHT7-coated rGO nanosheets loaded with the anticancer drug, doxorubicin (Dox).

2. Materials and methods

2.1. Synthesis of LHT7 and F-LHT7

LHT7 was synthesized according to a previously described method [19]. Briefly, ethylenediamine taurocholic acid (5 g) was dissolved in methanol (150 ml) in the presence of sodium hydroxide (5 g). After stirring for 2 h, the solution was precipitated with cold acetonitrile. The resulting precipitate, sodium ethylenediamine taurocholate, was washed with cold acetonitrile and freeze-dried. Five hundred milligrams of LMWH (Fraxiparin; Nanjing King-Friend Biochemical Pharmaceutical Company Ltd., Nanjing, China) was dissolved in distilled water in the presence of *N*-hydroxysuccinimide (126.6 mg). Then, *N*-ethyl-*N'*-(3-dimethylaminopropyl) carbodiimide hydrochloride (310 mg) and sodium ethylenediamine taurocholate (686 mg) was added consecutively into this solution. After an overnight reaction, the solution was precipitated, washed with cold methanol, and freeze-dried. The final product, LHT7, was obtained as a white powder.

For the synthesis of fluorescein isothiocyanate (FITC)-labeled LHT7 (F-LHT7), LHT7 (200 mg) was dissolved in 0.1 M borate buffer (pH 9.0). This solution was then mixed with 20 mg of FITC (Sigma-Aldrich Chemical Co., St. Louis, MO, USA), dissolved in anhydrous dimethyl sulfoxide (DMSO), and reacted for 5 h. The compound was washed twice with cold methanol and then dissolved in distilled water. The solution was purified by dialysis using a membrane with a molecular-weight cutoff of 2000 Da (Spectrum Laboratories Inc., Rancho Dominguez, CA, USA) and freeze-dried to yield the final product, F-LHT7.

2.2. Preparation of rGO nanosheets

rGO nanosheets were produced by reducing GO nanosheets. GO nanosheets were prepared from graphite using Hummer's method with slight modifications [14]. Briefly, graphite powder (0.5 g; Sigma-Aldrich), KMnO_4 (3 g; Sigma-Aldrich) and NaNO_3 (0.5 g; Sigma-Aldrich) were added to cold H_2SO_4 (23 ml), and the mixture was stirred initially on ice and then at 35 °C for an additional 1 h. After addition of 46 ml of triple-distilled water (TDW), the mixture was stirred at 90 °C for 1 h. The reaction was stopped by addition of 140 ml of TDW and 10 ml of 30% H_2O_2 . After washing, the reaction products were dispersed in TDW and sonicated for 2 h to exfoliate the GO layers and form GO nanosheets. Un-exfoliated GO was removed by centrifugation at 1600 \times g for 10 min. The supernatant containing GO nanosheets was collected and filtered through 0.2- μm polycarbonate membrane filters (Millipore Corp., Billerica, MA, USA) using an extruder (Northern Lipid, British Columbia, Canada).

For preparation of rGO nanosheets, the resulting GO nanosheets were reduced by adding 2.0 ml of GO nanosheets (5 mg/ml) in TDW to 8.0 ml of TDW, 0.5 ml of ammonia solution (28 w/w% in water; Junsei Chemical, Tokyo, Japan), and 5.0 μl of hydrazine monohydrate (64 w/w% in water; Sigma-Aldrich). The resulting mixture was stirred at 80 °C for 10 min. After cooling to room temperature, excess hydrazine and

ammonia were removed by dialysis (molecular weight cutoff, 100 kDa; Spectrum Laboratories, Inc.) against TDW. The obtained rGO nanosheets were stored at 4 °C until use.

2.3. Preparation and characterization of LHT-rGO nanosheets

For coating surfaces with LHT7, rGO nanosheets in TDW (1 mg/ml) were mixed with an equivalent volume of LHT7 solution (5 mg/ml) at a LHT7:rGO weight ratio of 5:1. Unloaded LHT7 was removed by gel filtration through a Sephadex G-25 M column (GE Healthcare, Piscataway, NJ, USA), yielding LHT-rGO nanosheets. The extent of LHT7 loading onto rGO was determined by measuring the decrease in F-LHT7 fluorescence at 525 nm caused by the quenching of adsorbed fluorophores by rGO using a fluorescence microplate reader (Gemini XS; Molecular Device, Sunnyvale, CA, USA). The size and morphology of LHT-rGO were examined by transmission electron microscopy (JEM1010; JEOL Ltd, Tokyo, Japan).

2.4. Stability test of LHT-rGO nanosheets

The stability of LHT-rGO nanosheets was tested in phosphate-buffered saline (PBS) (50 mM, pH 7.4) and fetal bovine serum (FBS; Gibco BRL Life Technologies, Carlsbad, CA, USA). An aliquot (0.1 ml) of rGO or LHT-rGO in TDW (rGO content, 0.5 mg/ml) was added to 0.9 ml of PBS, and the solutions were allowed to stand for 24 h. The stability of LHT-rGO nanosheets in PBS was evaluated by monitoring the mixtures for the appearance of precipitates using a digital camera (Canon PC1089; Canon Inc, Tokyo, Japan). For tests of LHT-rGO stability in serum, an aliquot (0.1 ml) of F-LHT-rGO in TDW (rGO content, 0.5 mg/ml) was added to 0.9 ml of RPMI-1640 media containing FBS (10%, 50%, or 90%), and the solutions were allowed to stand for 4 h. The stability of LHT-rGO complexes was determined by measuring the fluorescence of F-LHT7 released from LHT-rGO nanosheets using a fluorescence microplate reader (Gemini XS; Molecular Device).

2.5. Preparation of Dox-loaded nanosheets

Dox was loaded onto rGO and LHT-rGO nanosheets by physical adsorption. For drug loading, 1 ml of Dox solution (0.5 mg/ml; Sigma-Aldrich) was added to 1 ml of rGO or LHT-rGO nanosheets in TDW and stirred for 2 h at room temperature. Free Dox was then removed using a PD-10 desalting column (GE Healthcare), yielding Dox-loaded rGO (rGO/Dox) or Dox-loaded LHT-rGO (LHT-rGO/Dox). In some experiments, the resultant rGO/Dox or LHT-rGO/Dox were further eluted by the PD-10 desalting column, and the absorbance spectrum was measured using UV-vis spectrophotometry (UV-3100, Shimadzu Corp, Tokyo, Japan). The extent of Dox loading onto rGO and LHT-rGO nanosheets was determined by measuring the loss of Dox fluorescence at 485 nm caused by the quenching of adsorbed Dox by rGO or LHT-rGO using a fluorescence microplate reader (Gemini XS; Molecular Device).

2.6. Cellular uptake test of Dox delivered by LHT-rGO nanosheets

The cellular uptake of Dox was tested in human KB carcinoma cells using confocal microscopy. KB cells were seeded onto cover glasses at a density of 8×10^4 cells/well in 24-well plates. The next day, cells were treated with rGO/Dox or LHT-rGO/Dox at a concentration of 10 μM Dox. After incubating for 1 h, cells were washed and fixed with 4% paraformaldehyde in PBS for 15 min, and stained with 4',6-diamidino-2-phenylindole dihydrochloride (DAPI). The fluorescence of cellular Dox was observed using a confocal laser-scanning microscope (LSM 5 Exciter; Carl Zeiss, Inc., Jena, Germany).

2.7. *In vitro* antitumor efficacy study of Dox-loaded nanosheets

The *in vitro* antitumor efficacy of Dox on nanosheets was tested using cell viability assays. KB cells were seeded into 48-well plates at a density of 6×10^4 cells/well. The next day, cells were treated with rGO/Dox or LHT-rGO/Dox at a concentration of 3 μ M Dox. After 1 h, culture media were replaced with fresh media and cells were maintained for 24 h. Cell viability was measured using a Cell Counting Kit-8 (CCK-8; Dojindo, Tokyo, Japan) as described by the manufacturer. Briefly, 20 μ l of CCK-8 (water-soluble tetrazolium salt) solution was added to each well for 30 min, and absorbance was measured at 450 nm using a microplate reader (Sunrise-Basic TECAN, Männedorf, Switzerland). Cell viability in each group was expressed as a percentage of that in control cells.

2.8. *In vivo* molecular imaging

The *in vivo* distribution of 1,2-distearoyl-sn-glycero-3-phosphoethanolamine-N-(Alexa Fluor 680[polyethylene glycol]-5000) (DSPE-PEG₅₀₀₀-Alexa Fluor 680)-labeled LHT-rGO nanosheets to tumor tissues was tested by molecular imaging. Five-week-old female Balb/c and athymic nude mice (Orient Bio Inc., Seongnam, Kyonggi-do, Republic of Korea) were used for *in vivo* studies. All animals were maintained and used in accordance with the Guidelines for the Care and Use of Laboratory Animals of the Institute of Laboratory Animal Resources, Seoul National University (Seoul, Republic of Korea; approved animal experimental protocol number SNU-130129-3-1). The mice were subcutaneously inoculated at both dorsal sides with 2×10^6 KB cells. After tumors had become established, Dox (2.5 mg/kg) was intravenously administered in free form or on rGO or LHT-rGO nanosheets. After 1, 24 and 48 h, delivery efficiency was assessed using an eXplore Optix system (Advanced Research Technologies Inc., Montreal, Canada). For molecular imaging, rGO or LHT-rGO was labeled with DSPE-PEG₅₀₀₀-Alexa Fluor 680 by adding 10 mg DSPE-PEG₅₀₀₀-Alexa Fluor 680 to 2.5 mg/ml rGO or LHT-rGO. The fluorescent lipid labeling of rGO or LHT-rGO with DSPE-PEG₅₀₀₀-Alexa Fluor 680 was quantitated using an inorganic phosphate assay [20]. In brief, DSPE-PEG₅₀₀₀-Alexa Fluor 680 labeled-rGO or LHT-rGO were digested with 400 ml 5 M H₂SO₄ at 170 °C, and 100 ml 30% H₂O₂ was added to the cooled samples. The mixtures were heated at 170 °C until the H₂O₂ was completely removed. To the cooled sample, 4.6 ml of 0.2% ammonium molybdate and 100 ml of 15% fresh ascorbic acid were sequentially added while vortexing. The resulting mixtures were then boiled for 10 min at 100 °C, cooled to room temperature, and the absorbance was read at 830 nm. Standards were prepared with phosphorus standard solution (Sigma). Excitation and emission spots were raster-scanned in 1-mm steps over the region of interest to generate emission wavelength scans. A 670-nm pulsed-laser diode was used to excite Cy5.5 molecules. Long wavelength fluorescence emission (600–700 nm) was detected with a fast photomultiplier tube (Hamamatsu Photonics, Hamamatsu, Japan) and a time-correlated single photon counting system (Becker and Hickl GmbH, Berlin, Germany).

2.9. Drug localization and distribution study in tumor tissue

Drug localization and distribution within tumor tissue were observed by whole-mount staining of tumor tissue. Tumor-bearing mice were intravenously administered with rGO/Dox or LHT-rGO/Dox nanosheets labeled with DSPE-PEG5000-Alexa Fluor 680. In some experiments, mice were intravenously injected with FITC-labeled LHT7 in free form or on rGO/Dox nanosheets (FITC-LHT-rGO/Dox). Tumor tissues were collected 24 h post-dose and cut into 2×2 mm³ plugs using a scalpel. These tumor tissue pieces were then fixed in 25% DMSO in methanol for 24 h. After washing thoroughly with sterile PBS, plugs were incubated in PBS/3% bovine serum albumin containing 1% Tween-20 for 3 h at 4 °C with gentle agitation. The plugs were then incubated with phycoerythrin-labeled anti-CD31 antibody or with

DAPI (Thermo Fisher Scientific, San Jose, CA, USA) overnight at 4 °C with gentle agitation. Stained plugs were thoroughly washed again with sterile PBS and embedded in Pertex mounting medium (Histolab Products AB, Västra Frölunda, Sweden). The three-dimensional vascular structure and drug distribution within the tumor tissue were observed and imaged by confocal laser-scanning microscopy (LSM710; Carl Zeiss).

2.10. *In vivo* antitumor activity test

The antitumor effects of Dox were tested in KB tumor-bearing mice. Five-week-old athymic nude mice (Orient Bio, Inc.) were subcutaneously injected at the dorsal right side with 2×10^6 KB cells. When tumor volumes reached 150–180 mm³, mice were intravenously administered Dox and/or LHT7 in free form or on nanosheets. For systemic injection, mice were treated with Dox (1.25 mg/kg) alone or as a mixture with LHT7 (12.5 mg/kg). For comparison, mice were intravenously treated with plain rGO/Dox (2.5 mg/kg rGO, 1.25 mg/kg Dox), LHT-rGO (12.5 mg/kg LHT, 2.5 mg/kg rGO) or LHT-rGO/Dox (12.5 mg/kg LHT, 2.5 mg/kg rGO, 1.25 mg/kg Dox) nanosheets in PBS every 3 days for a total of three injections. Twenty-five days after tumor inoculation, tumor tissues were isolated and weighed, then fixed in 10% neutral buffered formalin and embedded in paraffin blocks for further histological evaluation. Tumor tissue sections (4 μ m thick) were immunostained with an anti-proliferating cell nuclear antigen (PCNA) antibody (Thermo Fisher Scientific) and subjected to terminal deoxynucleotidyl transferase dUTP nick-end labeling (TUNEL) assays (Millipore Corporation, Billerica, MA, USA) to determine cell-proliferation status and apoptosis, respectively. The numbers of proliferating and apoptotic cells were counted using the image analysis software, Image-Pro Plus Version 6.0 (Media Cybernetics, Inc., Rockville, MD, USA), after photographing five different fields at a magnification of 200 using an Eclipse TE2000-S microscope (Nikon, Tokyo, Japan).

2.11. Statistics

Analysis of variance (ANOVA) with Student–Newman–Keuls post hoc tests was used for statistical evaluation of experimental data. All statistical analyses were done using SigmaStat software (version 3.5; Systat Software, Richmond, CA, USA); a *p*-value <0.05 was considered significant.

3. Results

3.1. Characterization of LHT-rGO nanosheets

Surface coating of rGO by LHT7 was evaluated by monitoring the quenching of F-LHT7 by rGO (Fig. 1A). FITC fluorescence is “turned off” upon adhesion of F-LHT7 to rGO via the taurocholate anchoring moiety owing to the fluorescence-quenching feature of graphene nanosheets [14]. Consistent with this fluorescence-quenching phenomenon, the fluorescence intensity of FITC steadily decreased as the weight ratio of F-LHT7 to rGO decreased, a reduction interpreted as LHT7 loading onto rGO (Fig. 1B). At LHT7:rGO weight ratios of 1:1 and 1:5, 89.6% \pm 0.2% and 75.4% \pm 0.2% of added F-LHT7 were loaded onto rGO, respectively (Fig. 1C). TEM imaging of rGO (Fig. 1D) and LHT-rGO (Fig. 1E) nanosheets revealed the unique shape of graphene-based nanosheets.

3.2. Dispersion stability of LHT-rGO nanosheets

LHT-rGO showed greater dispersion stability in buffers and serum than rGO nanosheets (Fig. 2). Immediately after dispersion of LHT-rGO in PBS, rGO and LHT-rGO nanosheets with LHT7:rGO weight ratios less than 0.5:1 exhibited aggregation. Twenty-four hours after dispersion, LHT-rGO with a LHT7:rGO weight ratio of 1:1 formed aggregates; in contrast, LHT-rGO with LHT7:rGO weight ratios greater than 5:1

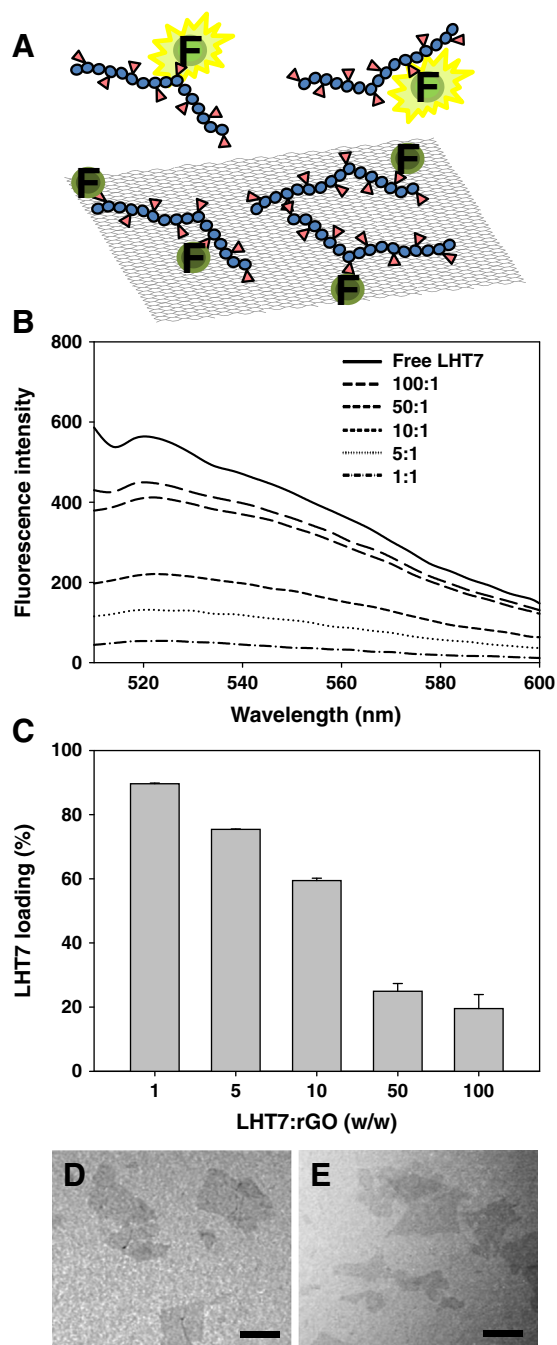


Fig. 1. Characterization of LHT7-rGO nanosheets. F-LHT7 adheres to rGO nanosheets, triggering fluorescence quenching (A). Interactions between rGO and F-LHT7 were analyzed by fluorometry (B), and the loading efficiency of F-LHT7 onto rGO was measured (C) at various weight ratios ($n = 4$). TEM images of uncoated rGO (D) and LHT-rGO (E) in which LHT was coated onto rGO at a 5:1 w/w ratio (E). Scale bar = 100 nm.

exhibited a stable dispersion at 24 h (Fig. 2A) that was maintained up to 3 d (data not shown). Moreover, LHT-rGO nanosheets with a LHT7:rGO weight ratio of 5:1 were stable in RPMI media supplemented with 10%, 50% or 90% FBS (Fig. 2B). Thus, a LHT7:rGO weight ratio of 5:1 was chosen for further experiments.

3.3. Loading of Dox onto LHT-rGO nanosheets

The Dox loading capacity of rGO and LHT-rGO nanosheets was evaluated by monitoring fluorescence quenching of Dox. Fluorescence quenching of Dox by rGO or LHT-rGO, manifesting as a decrease in

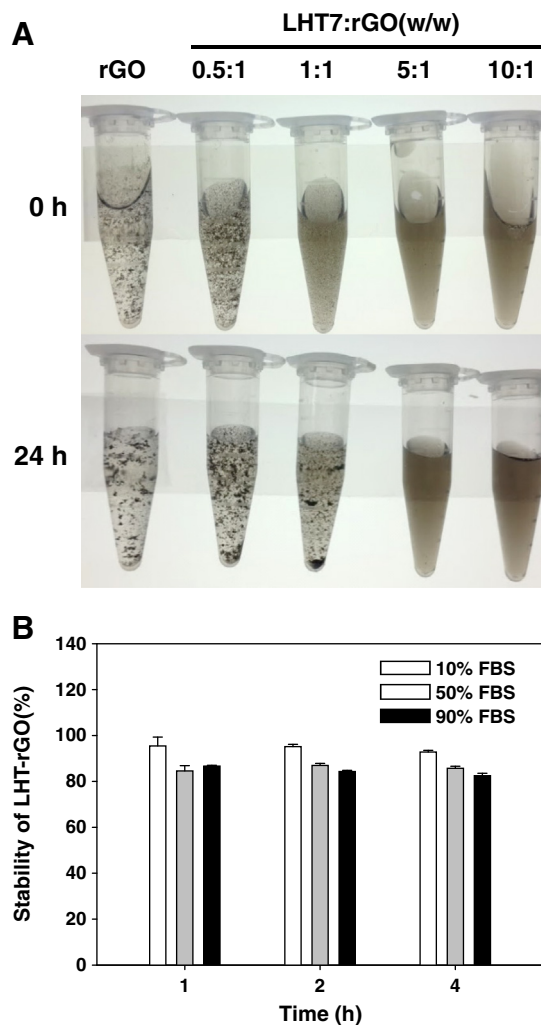


Fig. 2. Dispersion stability of LHT-rGO nanosheets in PBS and culture media. The stability of rGO and LHT-rGO nanosheet suspensions was evaluated in PBS (A). LHT-rGO with 5:1 w/w ratio was dispersed in RPMI media supplemented with 10%, 50% or 90% FBS (b).

fluorescence intensity, was greater at lower levels of added Dox and decreased as the amount of added Dox exceeded the loading capacity of the nanosheets (Fig. 3). LHT-rGO nanosheets showed a higher capacity for Dox loading compared with rGO nanosheets (Fig. 3A). At Dox:rGO weight ratios of 1:1, 2:1 and 5:1, almost complete quenching of Dox fluorescence (~90%) was observed with LHT-rGO nanosheets (Fig. 3B). In contrast, fluorescence quenching by rGO was only 73.1% \pm 2.1% at a Dox:rGO ratio of 1:1—indicating that the loading capacity of rGO was exceeded even at the lowest level of added Dox—and was further diminished at ratios of 2:1 (47.2% \pm 0.8%) and 5:1 (23.7% \pm 0.8%) (Fig. 3C). Dox-loaded LHT-rGO nanosheets are depicted in Fig. 3D.

3.4. Cellular uptake and anticancer efficacy of Dox delivered on LHT-rGO nanosheets

Dox on both plain rGO (rGO/Dox; Fig. 4C) and LHT-rGO (LHT-rGO/Dox; Fig. 4D) was effectively taken up by KB cells, as evidenced by direct detection of intracellular Dox fluorescence. These results were confirmed in experiments using rGO nanosheets labeled with DSPE-PEG₅₀₀₀-Alexa Fluor 680, which showed similar cellular uptake of rGO/Dox (Fig. 4E) and LHT-rGO/Dox (Fig. 4F). Merged fluorescence images of DAPI, Dox and DSPE-PEG₅₀₀₀-Alexa Fluor 680-labeled rGO (Fig. 4G) or DSPE-PEG₅₀₀₀-Alexa Fluor 680-labeled LHT-rGO (Fig. 4H) revealed that Dox and rGO differed in the intracellular distribution. Dox was co-localized to the nucleus, whereas rGO or LHT-rGO was

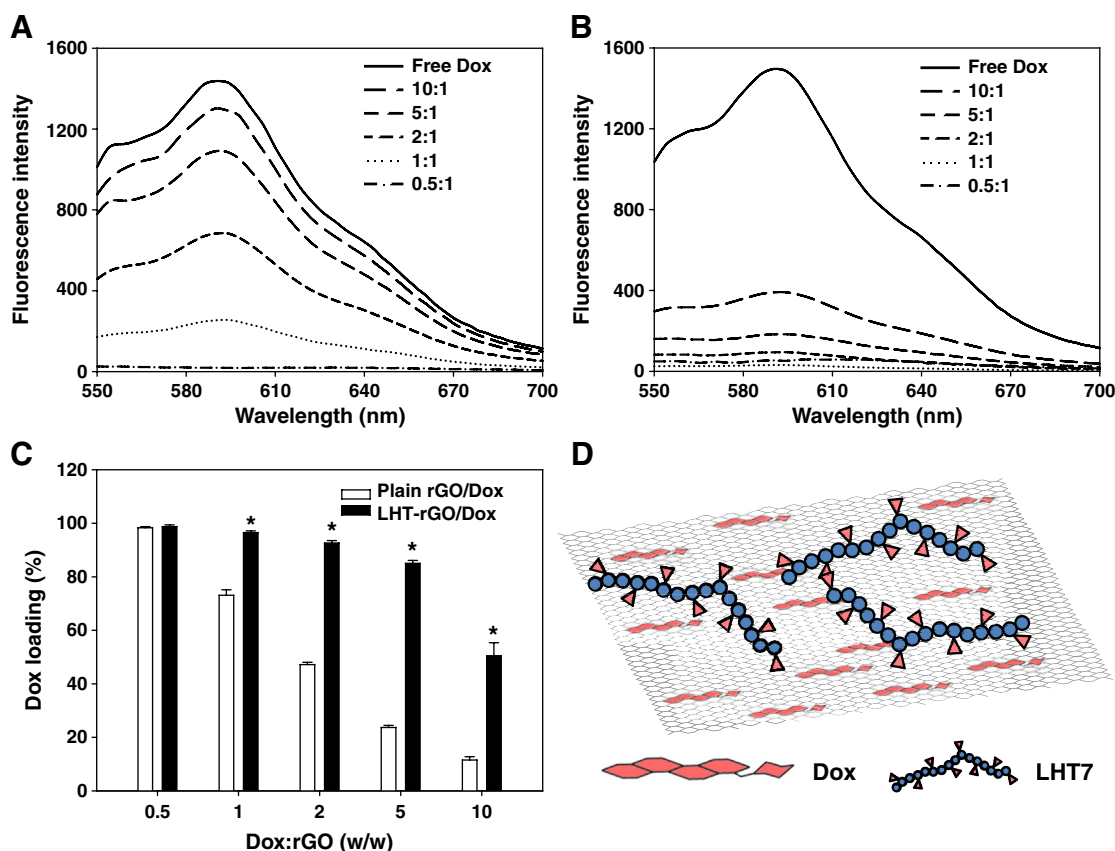


Fig. 3. Loading of Dox onto rGO or LHT-rGO nanosheets. Dox was loaded onto rGO (A) and LHT-rGO (B) nanosheets. Interactions between rGO or LHT-rGO and Dox were analyzed by fluorescence spectroscopy at various Dox:rGO weight ratios. The loading efficiency of Dox in complexes with rGO or LHT-rGO was measured (C). A schematic illustration of LHT-rGO/Dox is shown (D). (* $p < 0.05$ compared to the rGO group; t -test).

observed in the cytoplasm. Consistent with the results of cellular uptake experiments, the *in vitro* anticancer efficacy did not significantly differ between the two preparations, with LHT-rGO/Dox and rGO/Dox reducing KB cell viability to $38.9\% \pm 1.0\%$ and $40.2\% \pm 1.6\%$, respectively (Fig. 4i).

3.5. *In vivo* tumor tissue distribution of LHT-rGO/Dox

We next evaluated the tumor distribution of LHT-rGO/Dox and rGO/Dox following *in vivo* administration. At 1 h after dosing, the distribution at tumor sites was greater in LHT-rGO/Dox-treated mice than in rGO/Dox-treated mice (Fig. 5A), a difference that was maintained at 24 and 48 h post dose. At 48 h post dose, photon count measurements revealed that the tumor retention of LHT-rGO/Dox was 7-fold higher than that of rGO/Dox (Fig. 5B). To further investigate the location of LHT-rGO/Dox or rGO/Dox within tumor tissues, we used a phycoerythrin-labeled anti-CD31 antibody to visualize blood vessels (Fig. 6A and B). The distribution of DSPE-PEG₅₀₀₀-Alexa Fluor 680-labeled rGO/Dox to the tumor tissue was negligible (Fig. 6C). In contrast, intense distribution of DSPE-PEG₅₀₀₀-Alexa Fluor 680-labeled LHT-rGO/Dox to the tumor tissue was observed (Fig. 6D). The merged fluorescence images of blood vessels and fluorescent marker-labeled rGO nanosheets revealed that LHT-rGO/Dox did not stay in the tumor vasculature, but rather diffused into the tumor tissues at 24 h after injection (Fig. 6F). In addition, the colocalization of fluorescent LHT7 (Fig. 7A, B) with CD31-positive blood vessels (Fig. 7C, D) was observed for free LHT7 (Fig. 7E), and LHT-rGO/Dox (Fig. 7f). The distribution pattern of free LHT7 was limited to the blood vessels (Fig. 7E), whereas LHT-rGO/Dox distributed to the tumor tissues surrounding the blood vessels (Fig. 7F). Collectively, these imaging results reveal that LHT-rGO/Dox delivered to tumor

tissues diffuses from the tumor vasculature into the surrounding tumor cells.

3.6. *In vivo* antitumor effects of LHT-rGO/Dox

The *in vivo* antitumor efficacy of LHT-rGO/Dox was evaluated in a KB tumor xenograft model. On day 25 after tumor inoculation, tumor volumes (Fig. 8A) were significantly smaller in mice treated with LHT-rGO/Dox than in those treated with free Dox, LHT-rGO, rGO/Dox, or the mixture of free LHT7 and Dox. Consistent with this, tumor weights on day 25 were lowest in mice treated with LHT-rGO/Dox, which showed a $92.5\% \pm 3.1\%$ reduction in tumor weight compared with untreated mice (Fig. 8B).

The density of proliferating cells was proportional to the tumor volume and was lowest in mice treated with LHT-rGO/Dox (Fig. 9A and C). Moreover, although the number of apoptotic cells was significantly enhanced in all drug-treated groups compared to the control, the LHT-rGO/Dox-treated group showed the highest number of apoptotic cells. Compared to mice treated with a mixture of free LHT and Dox, the group treated with LHT-rGO/Dox showed a 2.4-fold increase in the number of apoptotic cells (Fig. 9B and D). Collectively, these results indicate that the antitumor activity of Dox was enhanced by delivery on LHT-rGO nanosheets.

4. Discussion

This study demonstrated that rGO coated with anti-angiogenic anticancer LHT7 is a much more effective alternative to rGO nanosheets for enhanced delivery of anticancer drugs to tumors. The coating of rGO with LHT7 improved physicochemical properties such as dispersion stability and Dox-loading capacity as compared with rGO nanosheets.

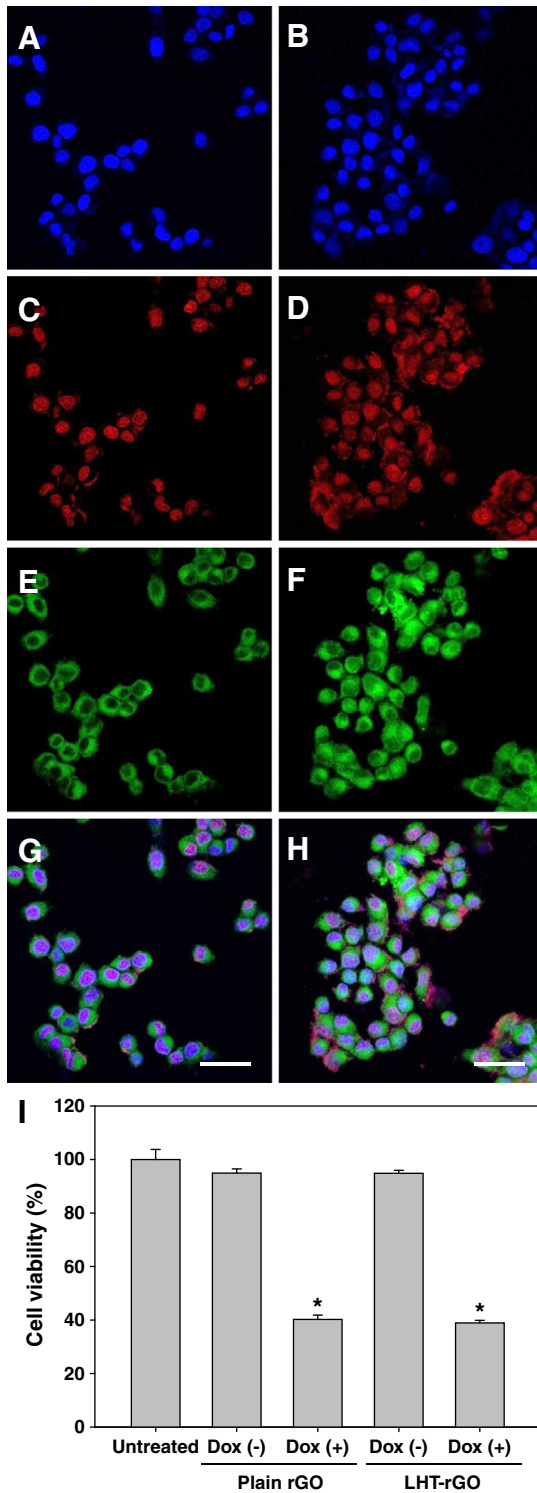


Fig. 4. Cellular uptake and antitumor effect of Dox delivered by nanosheets. KB cells were treated with Dox loaded onto rGO or LHT-rGO (DSPE-PEG₅₀₀₀-Alexa Fluor 680-labeled). One hour after treatment, the fluorescence images were obtained for DAPI stained on rGO/Dox (A) or LHT-rGO/Dox (B)-treated cells, for Dox delivered on rGO (C) or LHT-rGO (D), and for DSPE-PEG₅₀₀₀-Alexa Fluor 680 on rGO (E) or LHT-rGO (F). The merged fluorescence images of DAPI, Dox, and DSPE-PEG₅₀₀₀-Alexa Fluor 680-labeled rGO/Dox (G) or DSPE-PEG₅₀₀₀-Alexa Fluor 680-labeled LHT-rGO/Dox (H) were observed by confocal microscopy. Scale bar = 20 μ m. (I) For assessment of cancer cell killing effects, KB cells were treated with rGO or LHT-rGO, with or without Dox, and cell viability was quantified by CCK-8 assay ($n = 4$). (* $p < 0.05$ compared to untreated, rGO/Dox, and LHT-rGO/Dox groups; ANOVA and Student–Newman–Keuls test.).

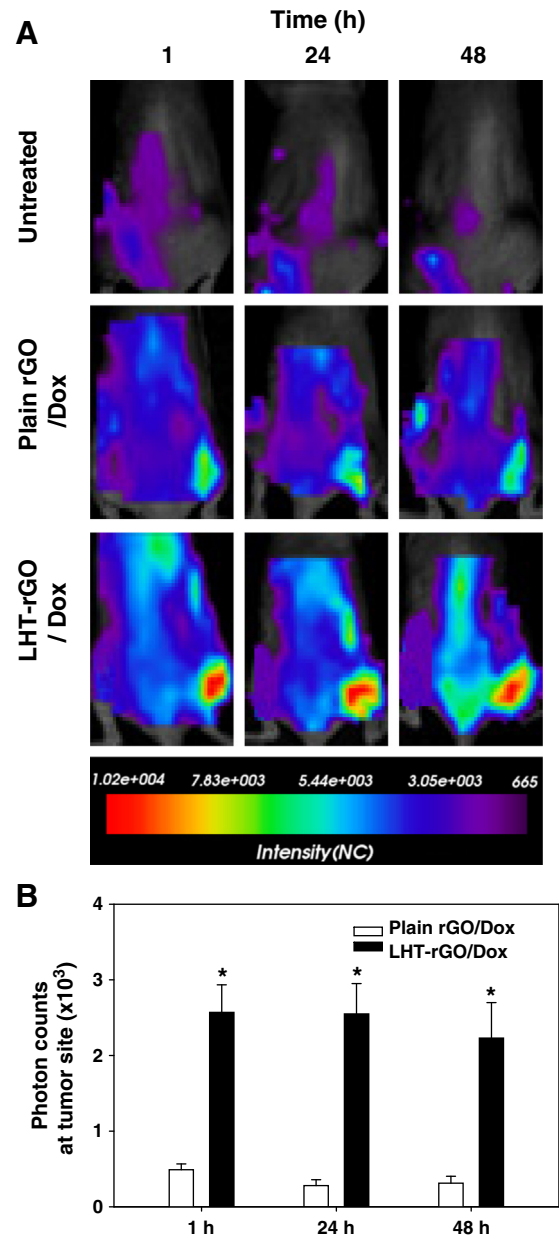


Fig. 5. *In vivo* biodistribution of LHT-rGO/Dox. KB tumor-bearing mice were intravenously administered 2.5 mg of Dox on rGO, or on LHT-rGO. For molecular imaging, both rGO and LHT-rGO were labeled with DSPE-PEG₅₀₀₀-Alexa Fluor 680. (A) At different times post injection (1, 24 and 48 h), the *in vivo* distribution of rGO/Dox and LHT-rGO/Dox was visualized using a molecular imaging system. (B) Quantification of average photon counts at the tumor site ($n = 4$). (* $p < 0.05$ compared to the rGO/Dox group; *t*-test.).

LHT-rGO was prepared by physical adsorption of LHT-7 onto rGO nanosheets. LHT7 was synthesized by conjugating the amine group of sodium ethylenediamine taurocholate with the carboxylic groups of LMWH at a molar ratio of 1 to 7 [17,18]. The sterane core of LHT7 belongs to the class of 4-cyclic compounds derived from steroids or sterols. The sterane core structure is known to confer binding affinity to rGO via hydrophobic interactions [21]. Thus, the seven-sterane structure of LHT7 conferred by taurocholate is expected to anchor LHT7 to rGO via hydrophobic interactions.

Surface modification with LHT-7 might also account for the greater dispersion stability of LHT-rGO nanosheets compared with rGO nanosheets (Fig. 2). It has previously been reported that coating of graphene nanosheets with unfractionated heparin increases their dispersion in water and enhances the anticoagulant activity of heparin [22]. Although

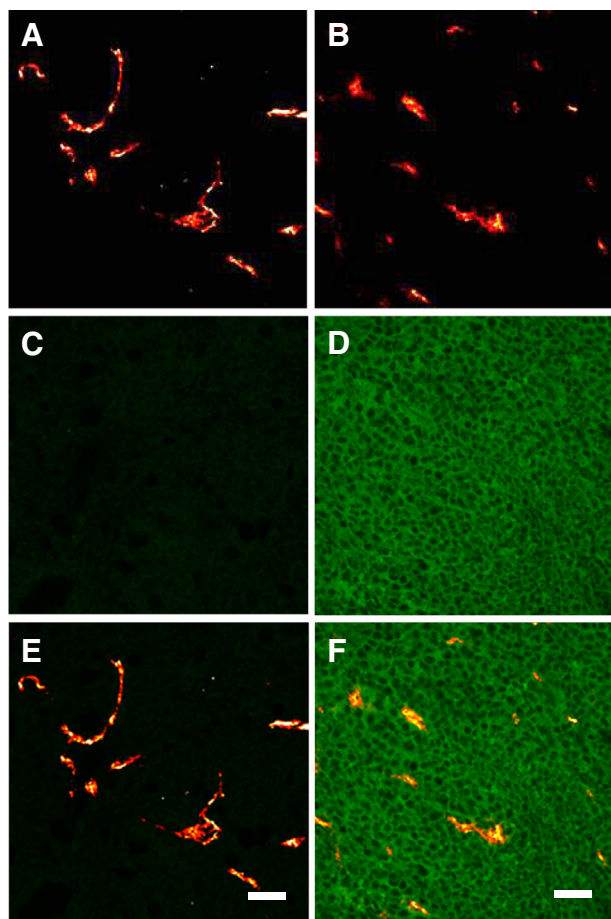


Fig. 6. Distribution of rGO/Dox and LHT-rGO/Dox in tumor tissues. KB tumor-bearing mice were intravenously administered with DSPE-PEG5000-Alexa Fluor 680-labeled rGO/Dox (A, C, E) or DSPE-PEG5000-Alexa Fluor 680-labeled LHT-rGO/Dox (B, D, F). After 24 h, tumor tissues were stained with phycoerythrin-labeled anti-CD31 antibody to label the tumor vasculature (A, B). The distribution of fluorescently labeled rGO/Dox (C) or LHT-rGO/Dox (D) inside tumor tissues was visualized using confocal microscopy. Merged fluorescence images of tumor vasculature with fluorescently labeled rGO/Dox (E) or LHT-rGO/Dox (F) are shown. Scale bar = 50 μm .

LHT-7 is derived from LMWH, LHT-7 differs from LMWH from the perspective of anticoagulant activity. Unlike LMWH, LHT-7 has been found to have little anticoagulant activity [18]. This lack of coagulant activity is desirable from the standpoint of using LHT-7 as a coating material for rGO nanosheets.

In this study, we separated rGO/Dox and LHT-rGO/Dox from free Dox using a desalting column. To test whether there was physical adsorption of rGO/Dox and LHT-rGO/Dox on the desalting column, we measured the UV spectrum of rGO/Dox and LHT-rGO/Dox after single and double elution through the desalting column. The similar UV absorbance spectra of single eluted and double-eluted rGO/Dox (Suppl. Fig. 1a) and LHT-rGO/Dox (Suppl. Fig. 1b) support that the physical adsorption of rGO/Dox or LHT-rGO/Dox onto the desalting column was negligible.

LHT-rGO nanosheets allowed higher Dox loading capacity compared with rGO nanosheets (Fig. 3C). Dox has been reported to bind graphene-based nanosheets and has been used as a model drug for pharmaceutical applications of graphenes [23–26]. While this affinity for graphene-based nanosheets enables Dox to bind uncoated rGO, the highly negatively charged LHT7 on LHT-rGO nanosheets may further bind positively charged Dox through electrostatic interaction, thereby increasing Dox loading capacity. Indeed, we recently reported increased loading efficiency of Dox on negatively charged hyaluronic acid-coated rGO via additional electrostatic interactions [14].

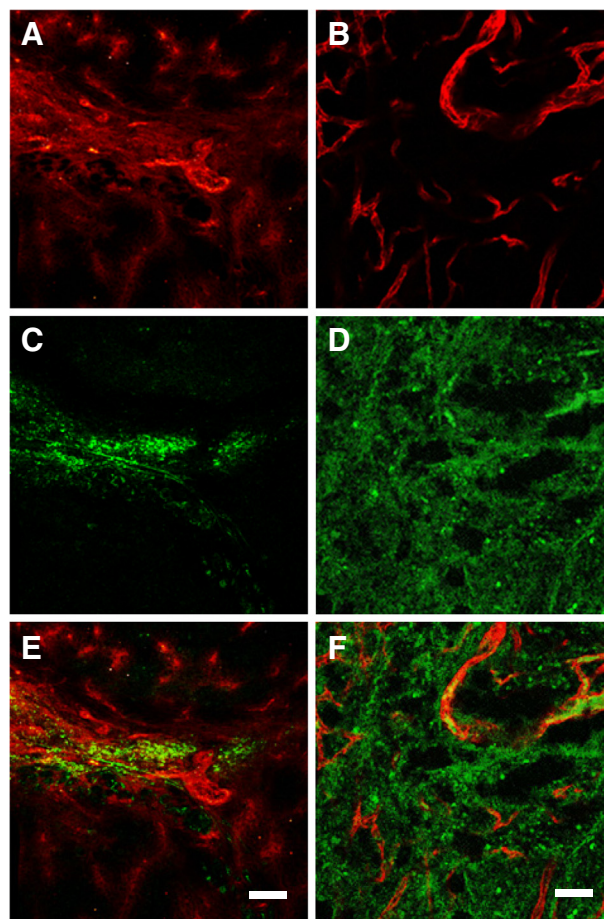


Fig. 7. Distribution of free LHT7 and LHT-rGO/Dox in tumor tissues. KB tumor-bearing mice were intravenously injected with FITC-labeled LHT7 alone (A, C, E) or FITC-LHT-rGO/Dox (B, D, F). After 24 h, tumor tissues were sectioned and stained with phycoerythrin-labeled anti-CD31 antibody to label the tumor vasculature (A, B). The distribution of free FITC-labeled LHT7 (C) or FITC-LHT-rGO/Dox (D) in tumor tissues was visualized using confocal microscopy. Merged images of tumor vasculatures with tumor tissue distribution of fluorescent LHT7 (E) or FITC-LHT-rGO/Dox (F) are shown. Scale bar = 50 μm .

For *in vivo* visualization the biodistribution of LHT-rGO nanosheets, we used DSPE-PEG-Alexa Fluor 680 as an imaging probe. The DSPE lipid moiety of the probe was used to anchor the probe onto rGO nanosheets via hydrophobic interaction. The attachment of DSPE-PEG-Alexa Fluor 680 onto rGO nanosheets was tested by the content of phosphate on rGO (Suppl. Fig. 2). After incubation of DSPE-PEG-Alexa Fluor 680 with rGO, the content of unattached DSPE-PEG-Alexa Fluor 680 in the supernatant was measured by the phosphate amount of DSPE. Suppl. Fig. 2 showed that more than 98% of DSPE-PEG-Alexa Fluor 680 was attached onto rGO, leaving less than 2% of free DSPE-PEG-Alexa Fluor 680 in the supernatant. Moreover, there was no difference in the loading efficiencies between rGO/Dox and LHT-rGO/Dox with the fluorescent lipid probe. Similar to this study, previous studies have used fluorescent lipid markers for *in vivo* imaging of graphenes [27,28].

It is notable that the enhanced anti-tumor effect of LHT-rGO/Dox over plain rGO/Dox was observed *in vivo* (Fig. 8), but not *in vitro* (Fig. 4). Consistent to the *in vitro* anti-tumor activity, the cellular uptake patterns did not differ between LHT-rGO/Dox and rGO/Dox. The discrepancy between *in vitro* and *in vivo* anti-tumor effect of LHT-rGO/Dox might be explained by the working mechanisms of LHT7. LHT7 has been reported to exert its anticancer effect by binding with angiogenic growth factors, such as vascular endothelial growth factor, that are highly expressed in tumor tissue environment [18]. Since the concentrations of angiogenic growth factors would be much lower in the

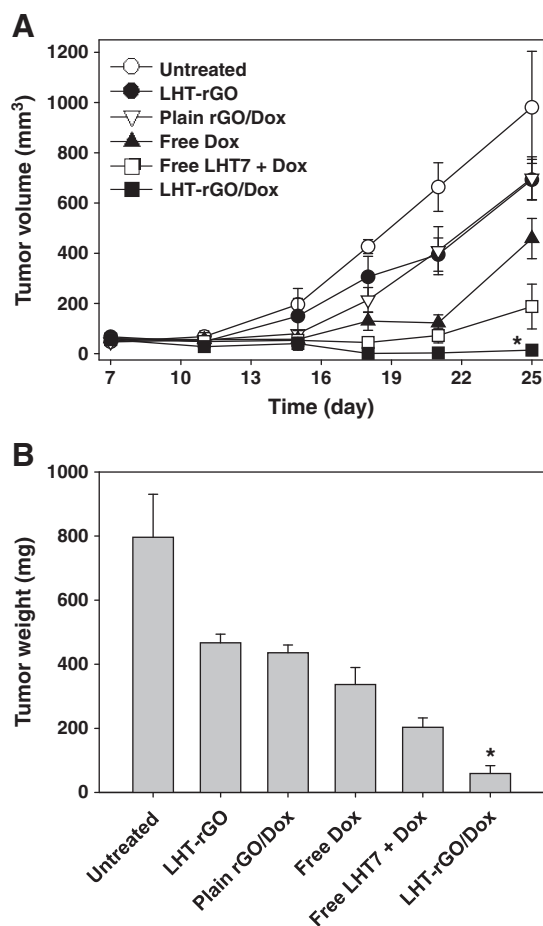


Fig. 8. *In vivo* antitumor efficacy of LHT-rGO/Dox. KB tumor-bearing mice (5 mice/group) were intravenously injected with Dox alone, a mixture of Dox with LHT7, rGO/Dox, or LHT-rGO/Dox in PBS every 3 day beginning on day 7. Tumor volumes were measured for each group (A). On day 25, tumor tissues were excised and weighed (B). (* $p < 0.05$ compared to other groups; ANOVA and Student–Newman–Keuls test).

cell culture medium as compared to the tumor microenvironment *in vivo*, LHT7-rGO/Dox might have little interaction with the growth factors. Such lack of interaction could have resulted in lack of synergistic anticancer effects with Dox in the cell culture system.

After cellular uptake of Dox-loaded rGO or LHT-rGO nanosheets, nucleus accumulation of Dox (Fig. 4C, D) was observed while rGO remained in cytoplasm (Fig. 4E, F). The nucleus localization of fluorescent Dox indicates that Dox might be liberated from rGO nanosheets. After loading onto rGO nanosheets, quenching of Dox was observed. The recovery of fluorescence intensity of Dox in the cell nucleus would be the result of dissociation of Dox from rGO in endolysosomes and diffusion of the liberated Dox from endolysosomes to the cytoplasm and finally to the nucleus. In a recent study, the release of Dox from GO nanosheets in the living cells was indeed observed by surface-enhanced Raman spectroscopy [29]. In the study, they reported that Dox was first liberated from GO nanosheets and escaped to the cytoplasm, and finally translocated to the nucleus. Unlike Dox, they observed that GO nanosheets were trapped in the cytoplasm. The retention of GO nanosheets in cytoplasm is possibly due to the size limitation of nuclear pore (less than 9 nm). Gold nanoparticles of 6 nm size were reported to be distributed to the nucleus of the cancer cells, whereas gold nanoparticles of 15 nm were shown to stay in the cytoplasm without entering the nucleus [30].

We observed the higher tumor tissue distribution of LHT-rGO/Dox compared with rGO/Dox. The enhanced tumor tissue distribution of LHT-rGO/Dox over rGO/Dox might be in part attributed to the enhanced stability of LHT-rGO/Dox in serum (Fig. 2B). Moreover, the diffusion of

LHT-rGO/Dox from tumor blood vessels into the tumor tissues (Fig. 6) supports the enhanced *in vivo* antitumor effects of Dox delivered with LHT-rGO (Fig. 8). The different tumor tissue distribution patterns of free LHT7 and LHT-rGO/Dox (Fig. 7) indicate that LHT7 were bound to rGO after delivery to the tumor vasculature, and diffused to the tumor tissues. Consistent with our observation, free heparin derivatives was reported to localize to vascular structures of tumor tissues [31].

This enhanced tumor tissue distribution and retention of LHT-rGO/Dox (Fig. 5) translated into significantly improved antitumor efficacy in KB tumor-bearing mice compared with rGO/Dox (Fig. 8). TUNEL assays showed that the population of apoptotic cells was highest in tumor tissues of LHT-rGO/Dox-treated mice (Fig. 9B), suggesting that apoptosis is likely the main mechanism by which LHT-rGO/Dox produces its antitumor effects. It is also possible that the anti-angiogenic anticancer activity of LHT7 on rGO could contribute to the enhanced antitumor activity. Indeed, LHT7 has been shown to bind angiogenic growth factors, like VEGF, and serve as a potential anti-angiogenic anticancer drug [18]. Moreover, liposomal co-delivery of LHT7 with an anticancer drug has been shown to produce a synergistic effect [19].

The greater antitumor effect of LHT-rGO/Dox compared with a mixture of free LHT7 and Dox underscores the importance of nanocarriers in chemotherapy. Recently, dendronized heparin–Dox conjugate-based nanoparticles were shown to exert improved antitumor activity in a 4T1 breast tumor model [32]. Compared with chemical conjugation of Dox, the physical adsorption of Dox onto LHT-rGO may have advantages. First, the absence of chemical modifications of the Dox structure may eliminate efficacy and safety concerns raised for chemically modified drugs. Moreover, the additional chemical conjugation step may increase nanomedicine manufacturing costs.

5. Conclusions

The surface coating of rGO with LHT7, a LMWH derivative with anti-angiogenic anticancer property, increased the dispersion stability of rGO in serum and enhanced its Dox-loading capacity through additional electrostatic interaction. Following systemic administration, LHT-rGO/Dox exhibited greater and more prolonged distribution to tumor tissues compared with rGO/Dox. Moreover, LHT-rGO/Dox effectively diffused from the tumor vasculature into the tumor tissues and exerted enhanced antitumor effects, possibly through both apoptosis and anti-angiogenic effects of LHT7. Collectively, our results support the potential application of LHT-rGO for the delivery of various anticancer drugs.

Acknowledgments

This work was supported by research grants from the Ministry of Science, ICT and Future Planning (NRF-2012R1A2A1A01007005, 2013K000264), and from the Business for Cooperative R&D between Industry, Academy, and Research Institute funded Korea Small and Medium Business Administration (No. C0010962).

Appendix A. Supplementary data

Supplementary data to this article can be found online at <http://dx.doi.org/10.1016/j.jconrel.2014.06.026>.

References

- [1] J. Liu, L. Cui, D. Losic, Graphene and graphene oxide as new nanocarriers for drug delivery applications, *Acta Biomater.* 9 (2013) 9243–9257.
- [2] L. Feng, L. Wu, X. Qu, New horizons for diagnostics and therapeutic applications of graphene and graphene oxide, *Adv. Mater.* 25 (2013) 168–186.
- [3] K. Yang, L. Feng, X. Shi, Z. Liu, Nano-graphene in biomedicine: theranostic applications, *Chem. Soc. Rev.* 2013 (42) (2013) 530–547.
- [4] M.C. Duch, G.R.S. Budinger, Y.T. Liang, S. Soberanes, D. Ulrich, S.E. Chiarella, et al., Minimizing oxidation and stable nanoscale dispersion improves the biocompatibility of graphene in the lung, *Nano Lett.* 11 (2011) 5201–5207.

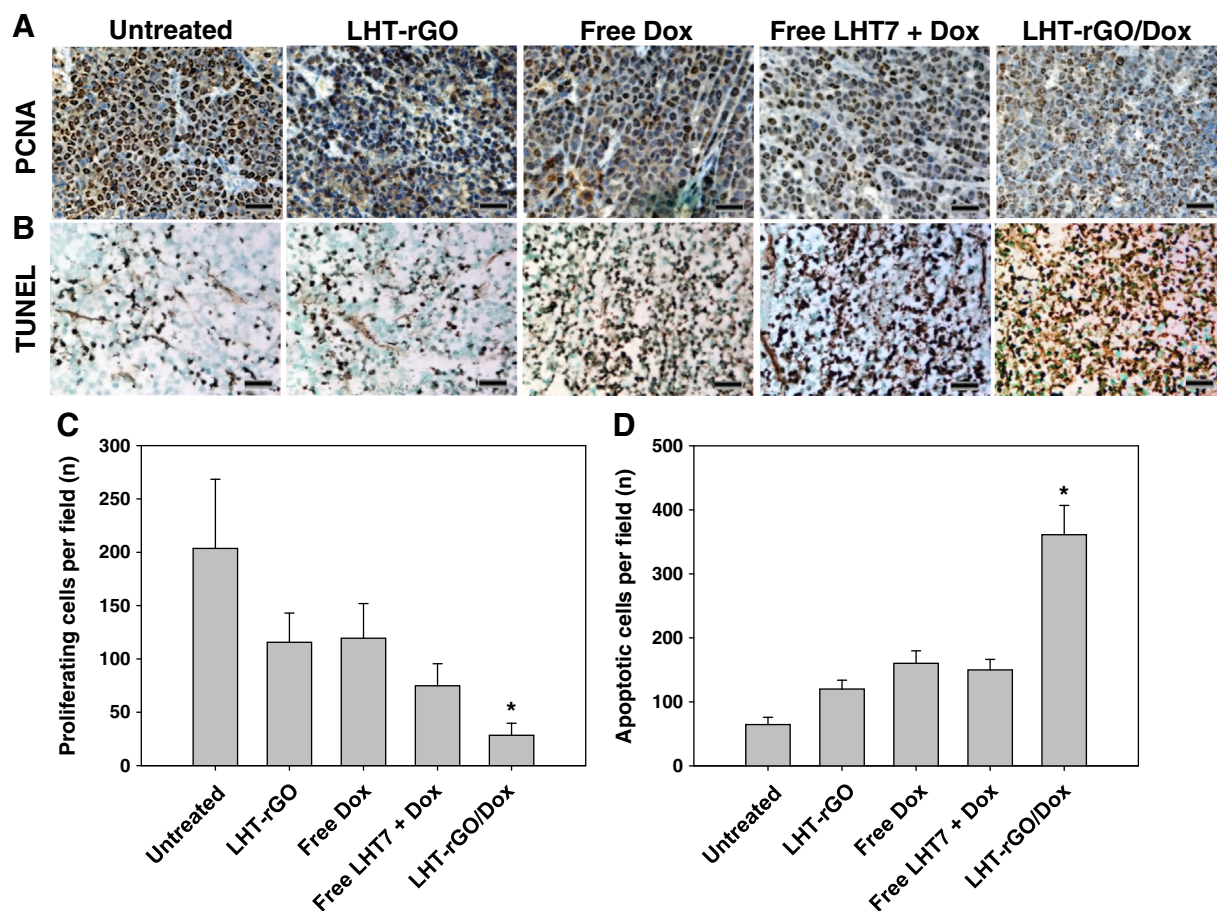


Fig. 9. Immunohistochemistry of tumor tissues. Tumor tissues were excised and sectioned for anti-PCNA antibody immunostaining (a) and TUNEL assay (b). The numbers of PCNA-immunostained proliferating cells (c) and TUNEL-labeled apoptotic cells (d) in isolated tumor tissues were determined ($n = 4$; * $p < 0.05$ compared to other groups; ANOVA and Student–Newman–Keuls test). Scale bar = 100 μm .

- H. Ali-Boucetta, D. Bitounis, R. Raveendran-Nair, A. Servant, J. Van den Bossche, K. Kostarelos, Graphene oxide: purified graphene oxide dispersions lack in vitro cytotoxicity and in vivo pathogenicity, *Adv. Healthc. Mater.* 2 (2013) 433–441.
- H.Y. Mao, S. Laurent, W. Chen, O. Akhavan, M. Imani, A.A. Ashkarran, et al., Graphene: promises, facts, opportunities, and challenges in nanomedicine, *Chem. Rev.* 113 (2013) 3407–3424.
- B.J. Hong, O.C. Compton, Z. An, I. Eryazici, S.T. Nguyen, Successful stabilization of graphene oxide in electrolyte solutions: enhancement of biofunctionalization and cellular uptake, *ACS Nano* 6 (2012) 63–73.
- M. Lotya, P.J. King, U. Khan, S. De, J.N. Coleman, High-concentration, surfactant-stabilized graphene dispersions, *ACS Nano* 4 (2010) 3155–3162.
- S. Lin, C.J. Shih, M.S. Strano, D. Blankschtein, Molecular Insights into the surface morphology, layering structure, and aggregation kinetics of surfactant-stabilized graphene dispersions, *J. Am. Chem. Soc.* 133 (2011) 12810–12823.
- C. Hou, H. Quan, Y. Duan, Q. Zhang, H. Wang, Y. Li, Facile synthesis of water-dispersible Cu_2O nanocrystal-reduced graphene oxide hybrid as a promising cancer therapeutic agent, *Nanoscale* 5 (2013) 1227–1232.
- K. Yang, L. Feng, H. Hong, W. Cai, Z. Liu, Preparation and functionalization of graphene nanocomposites for biomedical applications, *Nat. Protoc.* 8 (2013) 2392–2403.
- L. Zhang, Z. Wang, Z. Lu, H. Shen, J. Huang, Q. Zhao, et al., PEGylated reduced graphene oxide as a superior ssRNA delivery system, *Mater. Chem. B* 1 (2013) 749–755.
- H. Kim, D. Lee, J. Kim, T.I. Kim, W.J. Kim, Photothermally triggered cytosolic drug delivery via endosome disruption using a functionalized reduced graphene oxide, *ACS Nano* 7 (2013) 6735–6746.
- W. Miao, G. Shim, C.M. Kang, S. Lee, Y.S. Choe, H.G. Choi, et al., Cholesteryl hyaluronic acid-coated, reduced graphene oxide nanosheets for anti-cancer drug delivery, *Biomaterials* 34 (2013) 9638–9647.
- Y.K. Kim, M.H. Kim, D.H. Min, Biocompatible reduced graphene oxide prepared by using dextran as a multifunctional reducing agent, *Chem. Commun.* 47 (2011) 3195–3197.
- Y. Wang, P. Zhang, C. Fang, C. Liu, L. Zhan, Y.F. Li, et al., Green and easy synthesis of biocompatible graphene for use as an anticoagulant, *RSC Adv.* 2 (2012) 2322–2328.
- E. Lee, Y.S. Kim, S.M. Bae, S.K. Kim, S. Jin, S.W. Chung, et al., Polyproline-type helical-structured low-molecular weight heparin (LMWH)-taurocholate conjugate as a new angiogenesis inhibitor, *Int. J. Cancer* 124 (2009) 2755–2765.
- S.W. Chung, M. Lee, S.M. Bae, J. Park, O.C. Jeon, H.S. Lee, Potentiation of anti-angiogenic activity of heparin by blocking the ATIII-interacting pentasaccharide unit and increasing net anionic charge, *Biomaterials* 33 (2012) 9070–9079.
- J.Y. Kim, G. Shim, H.W. Choi, J. Park, S.W. Chung, S. Kim, et al., Tumor vasculature targeting following co-delivery of heparin-taurocholate conjugate and suberoylanilide hydroxamic acid using cationic nanolipoplex, *Biomaterials* 33 (2012) 4424–4430.
- Y.K. Oh, M.Y. Kim, J.Y. Shin, T.W. Kim, M.O. Yun, S.J. Yang, et al., Skin permeation of retinol in tween 20-based deformable liposomes: in-vitro evaluation in human skin and keratinocyte models, *J. Pharm. Pharmacol.* 58 (2006) 161–166.
- M. Swierczewska, K.Y. Choi, E.L. Mertz, X. Huang, F. Zhang, L. Zhu, et al., A facile, one-step nanocarbon functionalization for biomedical applications, *Nano Lett.* 12 (2012) 3613–3620.
- D.Y. Lee, Z. Khatun, J.H. Lee, Y.K. Lee, I. In, Blood compatible graphene/heparin conjugate through noncovalent chemistry, *Biomacromolecules* 12 (2011) 336–341.
- G. Liu, H. Shen, J. Mao, L. Zhang, Z. Jiang, T. Sun, et al., Transferrin modified graphene oxide for glioma-targeted drug delivery: in vitro and in vivo evaluations, *ACS Appl. Mater. Interfaces* 5 (2013) 6909–6914.
- W. Miao, G. Shim, S. Lee, Y.S. Choe, Y.K. Oh, Safety and tumor tissue accumulation of pegylated graphene oxide nanosheets for co-delivery of anticancer drug and photosensitizer, *Biomaterials* 34 (2013) 3402–3410.
- Y. Wang, R. Huang, G. Liang, Z. Zhang, P. Zhang, S. Yu, et al., MRI-visualized, dual-targeting, combined tumor therapy using magnetic graphene-based mesoporous silica, *Small* 10 (2013) 109–116.
- F. Wang, B. Liu, A.C. Ip, J. Liu, Orthogonal adsorption onto nano-graphene oxide using different intermolecular forces for multiplexed delivery, *Adv. Mater.* 25 (2013) 4087–4092.
- C. Peng, W. Hu, Y. Zhou, C. Fan, Q. Huang, Intracellular imaging with a graphene-based fluorescent probe, *Small* 6 (2010) 1686–1692.
- J.T. Robinson, S.M. Tabakman, Y. Liang, H. Wang, H.S. Casalogue, D. Vinh, et al., Ultrasmall reduced graphene oxide with high near-infrared absorbance for photothermal therapy, *J. Am. Chem. Soc.* 133 (2011) 6825–6831.

- [29] J. Huang, C. Zong, H. Shen, Y. Cao, B. Ren, Z. Zhang, Tracking the intracellular drug release from graphene oxide using surface-enhanced raman spectroscopy, *Nanoscale* 5 (2013) 10591–10598.
- [30] K. Huang, H. Ma, J. Liu, S. Huo, A. Kumar, T. Wei, et al., Size-dependent localization and penetration of ultrasmall gold nanoparticles in cancer cells, multicellular spheroids, and tumors in vivo, *ACS Nano* 6 (2012) 4483–4493.
- [31] S.M. Bae, J.H. Kim, S.W. Chung, Y. Byun, S.Y. Kim, B.H. Lee, et al., An apoptosis-homing peptide-conjugated LMWH-taurocholate conjugate with antitumor properties, *Biomaterials* 34 (2013) 2077–2086.
- [32] W. She, N. Li, K. Luo, C. Guo, G. Wang, Y. Geng, et al., Dendronized heparin–doxorubicin conjugate based nanoparticle as pH-responsive drug delivery system for cancer therapy, *Biomaterials* 34 (2013) 2252–2264.